Supplementary Information

Transition from the Wenzel to Cassie-Baxter state by PFOTES/TiO_2 nanoparticles leading to a mechanically robust and damage/contamination-recoverable surface

Ki Joon Heo[1,2,†], Jae Hyun Yoo[3],†, Juhun Shin[1], Wei Huang[4, 5], Manish K. Tiwari[3, 5], Jae Hee Jung[6], Ivan P. Parkin[1], Claire J. Carmalt[1], and Gi Byoung Hwang[1,*]

[1]Department of Chemistry, University College London, London WC1H 0AJ, United Kingdom

[2]School of Mechanical Engineering, Chonnam National University, Gwangju 61186, Republic of Korea

[3]Lab. M. 0, 47-24, Achasan-ro 15-gil, Seongdong-gu, Seoul 04799, Republic of Korea

[4]Nanoengineered Systems Laboratory, UCL Mechanical Engineering, University College London, London WC1E 7JE, United Kingdom

[5]Wellcome/EPSRC Centre for Interventional and Surgical Sciences, University College London, London W1W 7TS, United Kingdom

[6]Department of Mechanical Engineering, Sejong University, Seoul 05006, Republic of Korea

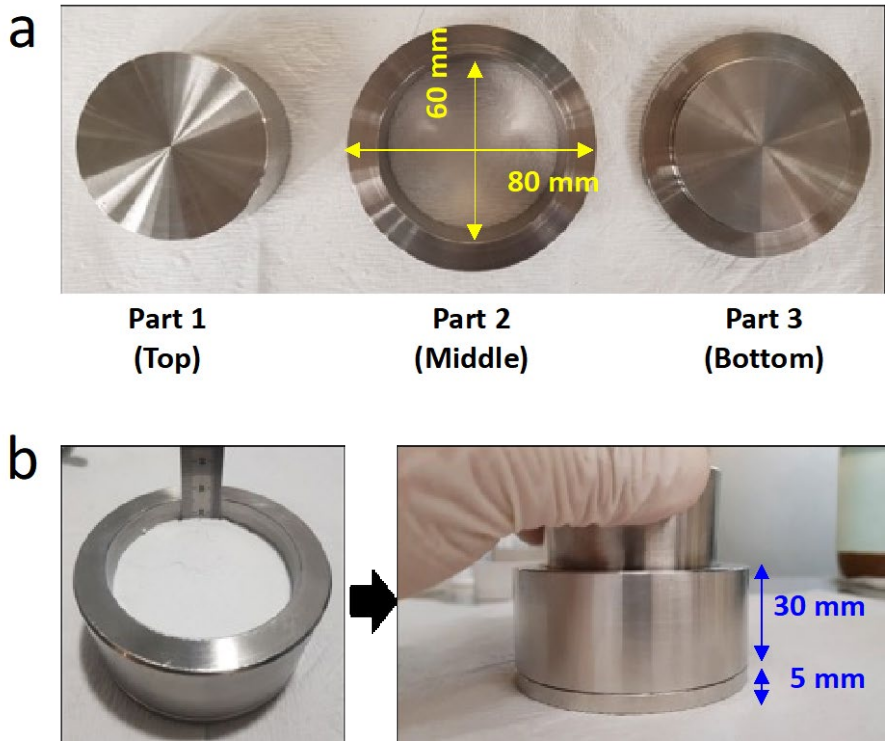

Fig. S1| (a) Mould composition and (**b**) powder addition and mould assembly

Supplementary Note 1

To confirm the functionalisation of hydrophilic titanium dioxide (TiO_2) nanoparticles (NPs) using 1H, 1H, 2H, 2H-perfluorooctyltriethoxysilane (PFOTES), Transmission Electron Microscope (TEM) analysis was employed. Figures S2a and b show the TEM images of the TiO_2 NPs before and after PFOTES treatment. The TiO_2 NPs, which are 12-20 nm in size, did not have a significant change in their shape and size after the PFOTES treatment. EDS spectra show the presence of silicon and fluorine on the TiO_2 NPs after PFOTES treatment (Figs. S2c and d), indicating a PFOTES bonding to the TiO_2 surface.

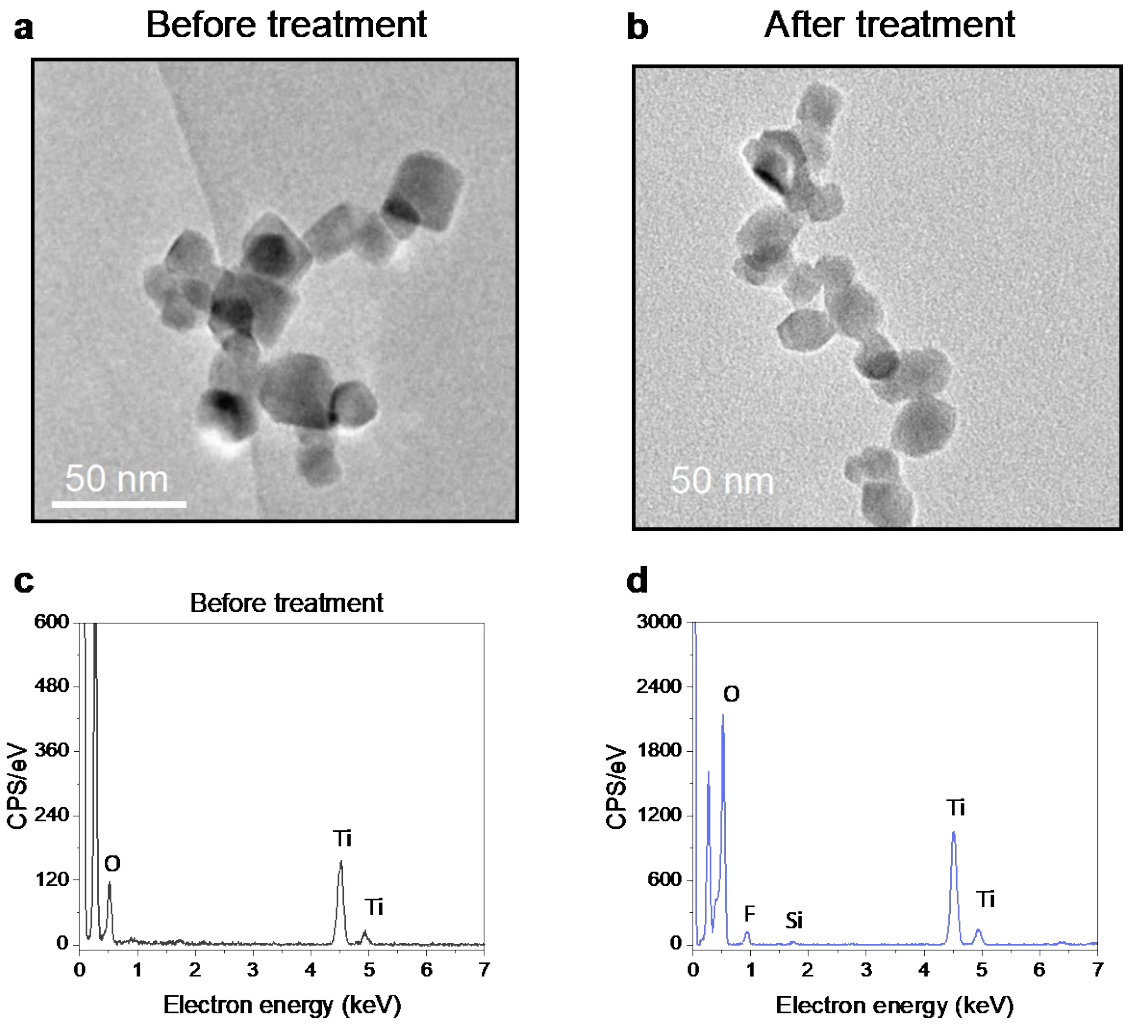

Fig. S2| Transmission Electron Microscope (TEM) of the TiO_2 nanoparticles **a**, before and **b**, after PFOTES treatment. Energy-dispersive X-ray spectroscopy (EDX) spectra of the TiO_2 nanoparticles **c**, before and **d**, after PFOTES treatment.

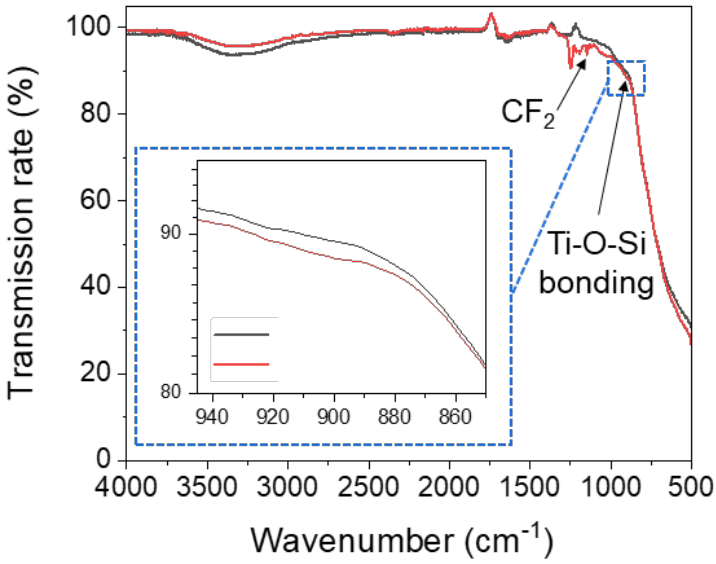

Fig. S3| Attenuated total reflectance infrared spectra of TiO_2 nanoparticles before and after PFOTES treatment.

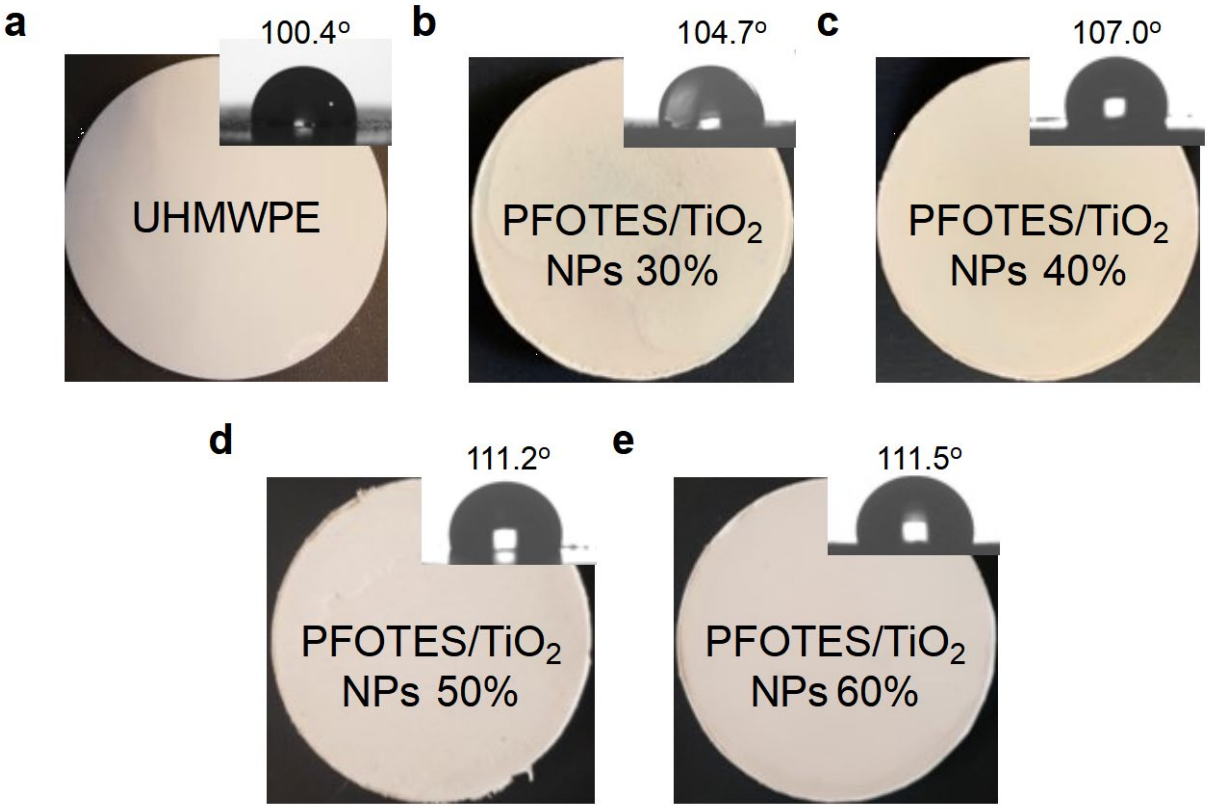

Fig. S4| Images and water contact angles of samples. **a**, UHMWPE. **b-e,** composites containing 30, 40, 50, and 60% PFOTES/TiO_2 NPs. The samples were produced through a thermal compression process at ~11 MPa and 150°C for 45 min. All the samples have a smooth surface.

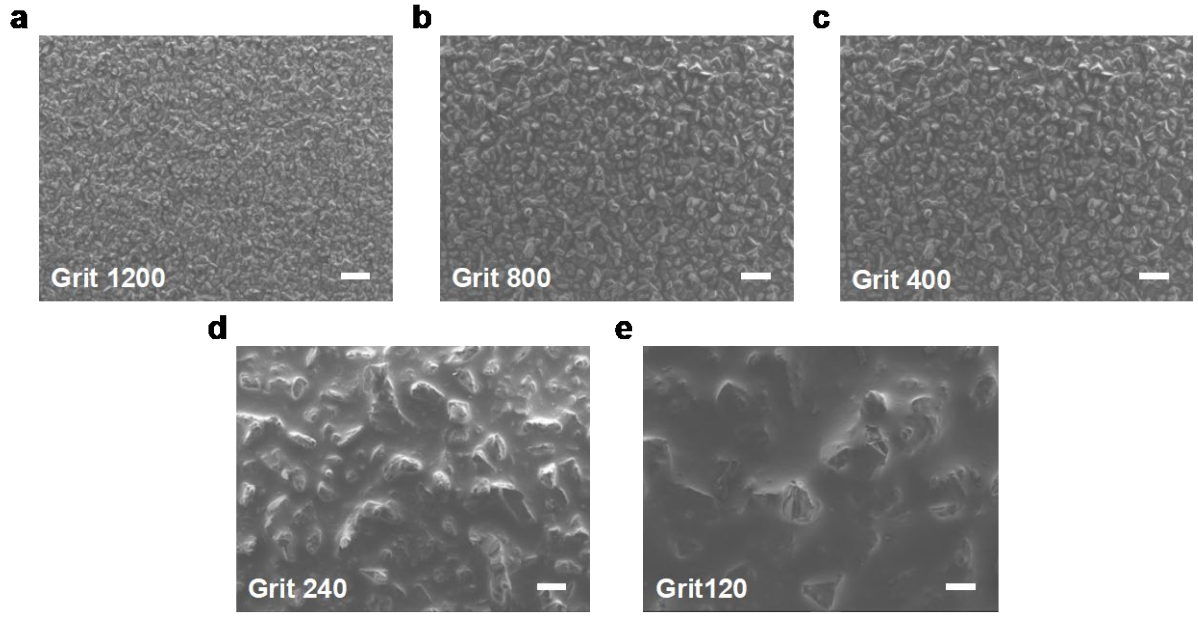

Fig. S5| SEM images for surface topographies of sandpapers. a-e, Grit No. 120, 240, 400, 800, and 1200 sandpapers (the scale bar length = 100 μm).

Supplementary Note 2

As shown in Figure S6−7, Rough surfaces were produced using the sandpaper abrasion process. The surface roughness on all samples increased by reducing the grit number of sandpaper. The surface roughness on all samples was highest when sandpaper with Grit, No. 120 was used. The roughness deviation for all samples treated using the sandpaper with Grit, No. #120 was ~12%, and the standard deviation for each condition was <10%. In addition, there was no statistical difference between all samples treated using sandpaper with Grit. No. 120 (t-test: p-value > 0.1). This result is similar to previous studies that fabricate the rough surface using sandpaper abrasions. Akid et al. (2015) showed that the surface roughness of composite epoxy/sol-gel materials increased with the decreasing grit number of the used sandpaper.[1] The standard deviation of the roughness was ~10%. Kanyanthare et al. (2020) also showed that after surface abrasion using sandpapers with grit No 320 and 1200, the surface roughness of PP, PE, PA, PS, and LDPE plastic samples increased, and their deviation was less than 15%.[2] This indicates that sandpaper abrasion produces a rough surface with a minor deviation.

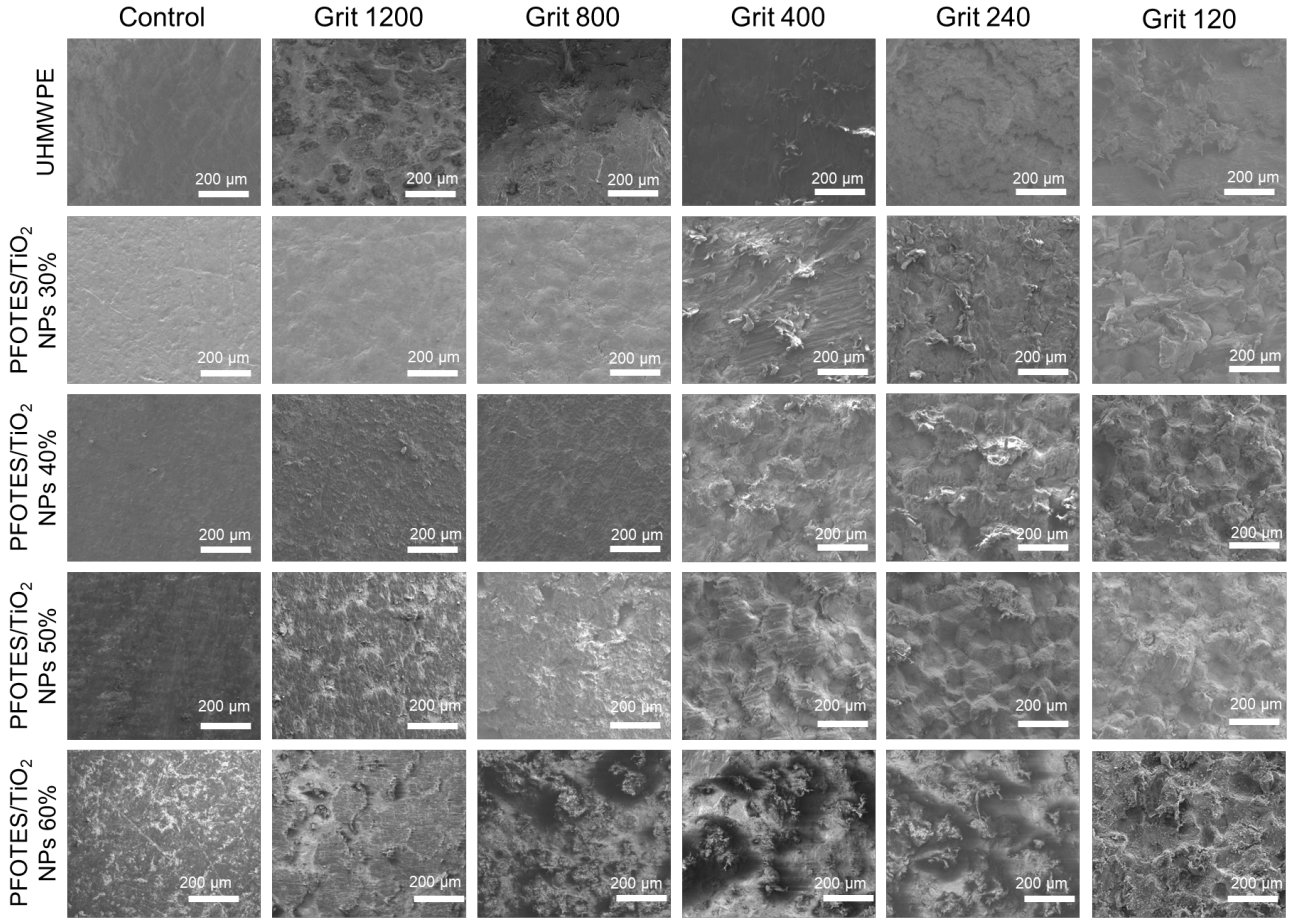

Fig. S6 |Surface topographies (SEM images) of UHMWPE and composites containing 30, 40, 50, and 60% PFOTES/TiO_2 NPs after the sandpaper abrasions (the scale bar length = 200 μm).

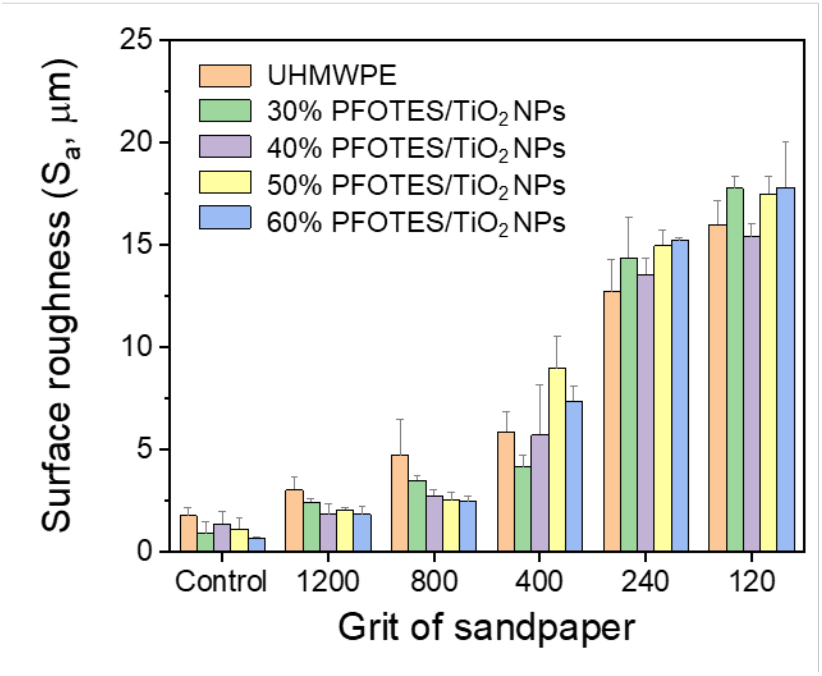

Fig. S7| Surface roughness of UHMWPE and composites containing 30, 40, 50 and 60% PFOTES/TiO_2 NPs after the sandpaper abrasions. Data presented as mean ± standard deviation.

Supplementary Note 3

To understand the surface wettability of the tested samples, the Wenzel and Cassie-Baxter models were applied to the experimental data. Figure S8 shows the correlation between experimental results and the Wenzel model calculations. Based on the statistical analysis, it was supposed that the surface roughness values of the samples under the same sandpaper were identical. The angle change of UHMWPE by the surface roughness increment complies with the Wenzel model. However, the composites containing PFOTES/TiO_2 NPs did not fit the model, indicating that the surface wetting of the composites is different from the Wenzel state. To further understand the composites, the Cassie-Baxter model was applied to the results, and plastron effects, which are observed on superhydrophobic surfaces in the Cassie-Baxter state, were investigated. As shown in Figure S9, the contact angle increase of the composites well fits the Cassie model. A silver mirror-like surface appears when the superhydrophobic surface immersed in water is at a glancing angle because of light reflection.[3] This is attributed to the air bubble layer between the liquid and superhydrophobic surface, known as the plastron effect.[4] As shown in Figure S10, the plastron effects were observed on superhydrophobic surfaces with 40, 50, and 60% PFOTES/TiO_2 NPs, indicating that they are in the Cassie-Baxter states. Despite fitting the Cassie model, the composite containing 30% PFOTES/TiO_2 NPs did not have a uniform plastron effect across the surface and a low contact angle hysteresis and rolling off-angle. Thus, it is considered that the surface is in an intermediate region between the Wenzel and Cassie-Baxter state.

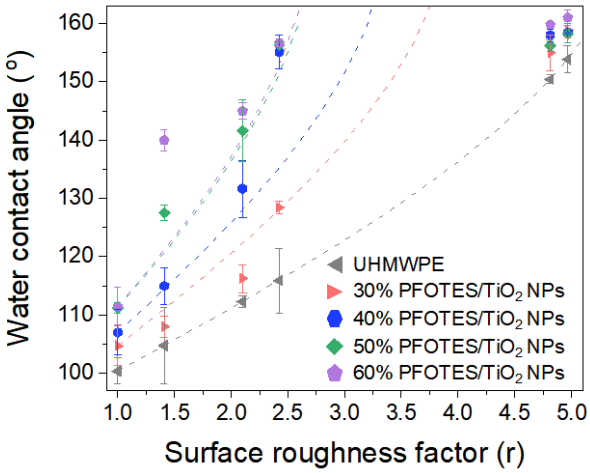

Fig. S8| Application of the Wenzel model to changes in the water contact angle of UHMWPE and composites containing 30, 40, 50 and 60% PFOTES/TiO_2 NPs by surface roughness increment. Data presented as mean ± standard deviation.

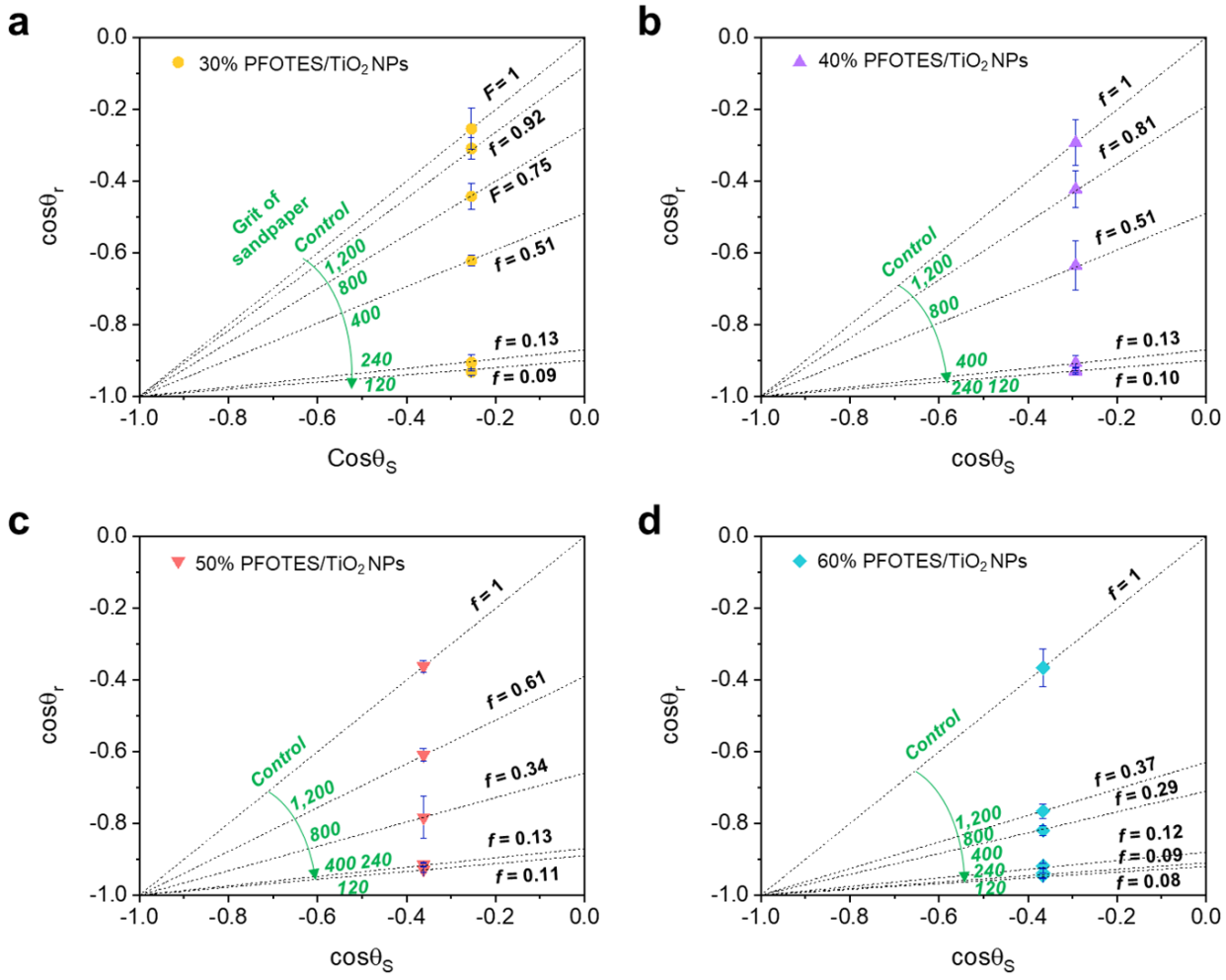

Fig. S9| Application of the Cassie-Baxter model to changes in the water contact angle of composites containing (**a**) 30, (**b**) 40, (**c**) 50 and (**d**) 60% PFOTES/TiO_2 NPs by surface roughness increment. Data presented as mean ± standard deviation.

Fig. S10| Plastron effect of UHMWPE and composites containing 30, 40, 50 and 60% PFOTES/TiO_2 NPs which have a water contact angle of >150°. The samples with a S_a of > 16 μm were used for the plastron effect test.

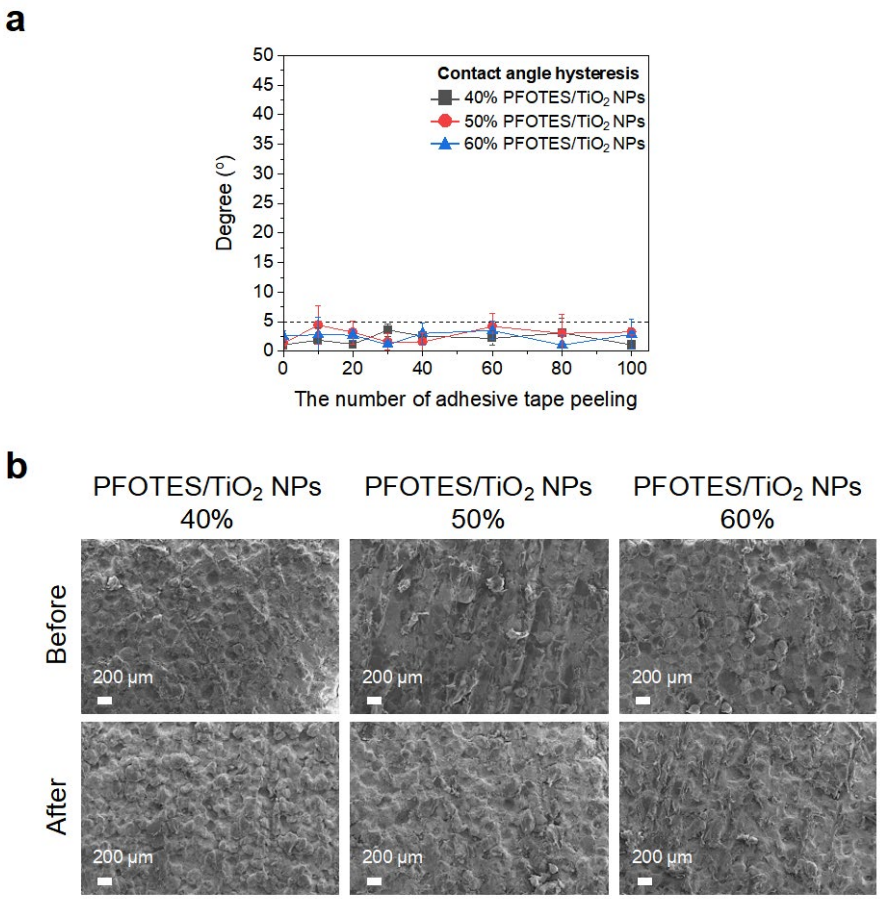

Fig. S11| 100 cycled adhesive tape peeling of superhydrophobic surfaces containing 40, 50 and 60% PFOTES/TiO_2 NPs. a, Contact angle hysteresis and **b**, Surface topographies (SEM images) of superhydrophobic surfaces before and after 100 cycled adhesive tape peeling. Data presented as mean ± standard deviation.

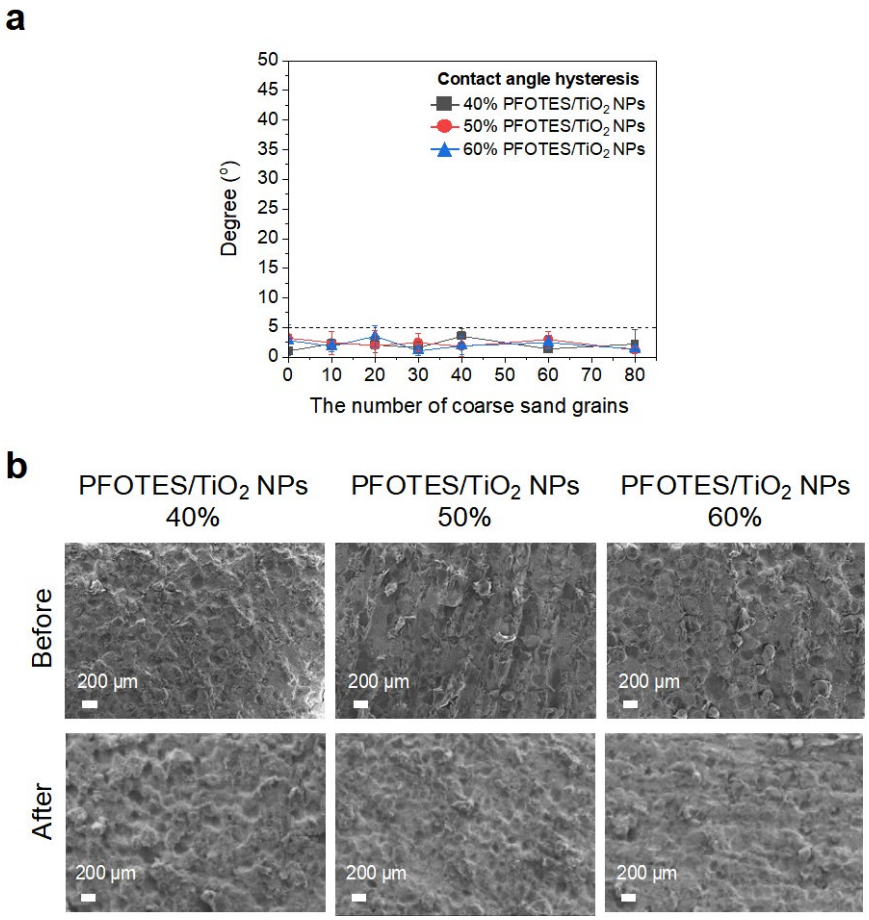

Fig. S12| 80 cycled sand grains dropping of superhydrophobic surfaces containing 40, 50 and 60% PFOTES/TiO_2 NPs. a, Contact angle hysteresis and **b**, Surface topographies (SEM images) of superhydrophobic surfaces before and after sand grains dropping. Data presented as mean ± standard deviation.

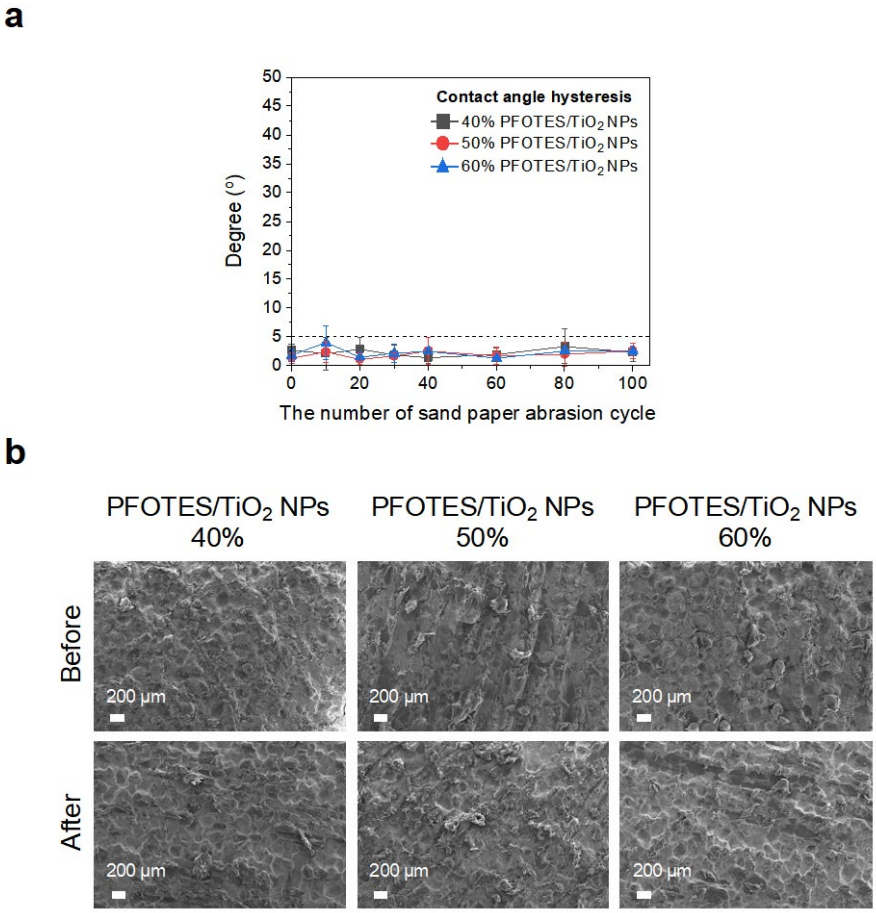

Fig. S13| 100 cycled sandpaper abrasion of superhydrophobic surfaces containing 40, 50 and 60% PFOTES/TiO_2 NPs. a, Contact angle hysteresis and **b**, Surface topographies (SEM images) of superhydrophobic surfaces before and after 100 cycled sandpaper abrasion. Grit No. 80 sandpaper was used for the abrasion test. Data presented as mean ± standard deviation.

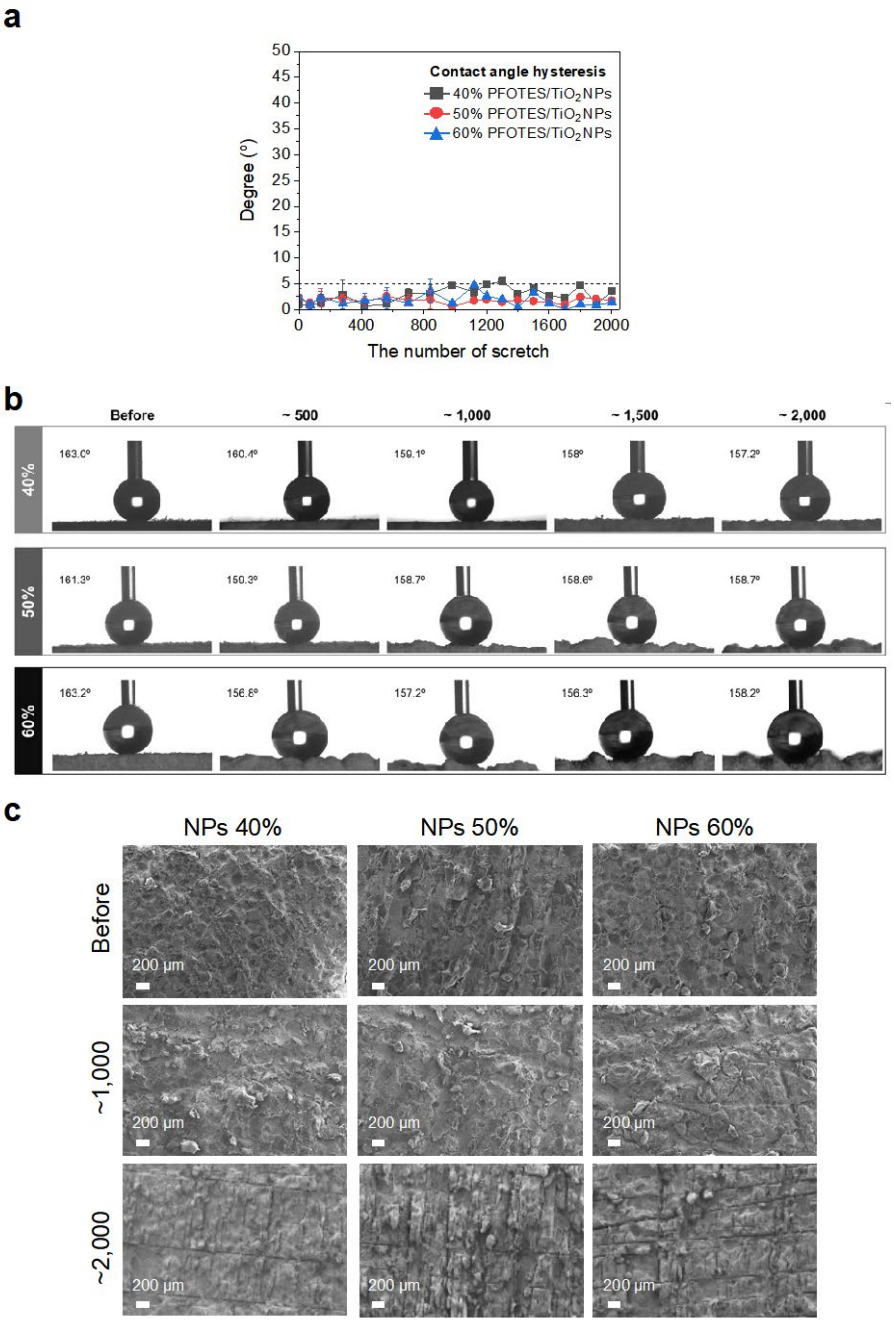

Fig. S14| 2000 times scalpel scratches of superhydrophobic surfaces containing 40, 50 and 60% PFOTES/TiO_2 NPs. **a**, Contact angle hysteresis. **d**, Surface damage progress for the 2000 times scratches. **d**, Surface topographies (SEM images) of superhydrophobic surface before and after 1,000- and 2,000-times scalpel scratches. Data presented as mean ± standard deviation.

Supplementary Note 4

Repellency against water droplets with pH 1-13

Figure S15 shows water contact angle, rolling off-angle and contact angle hysteresis of superhydrophobic surfaces containing 40, 50, and 60% PFOTES/TiO_2 NPs against water droplets with pH 1-13. The water contact angles of the surfaces were not affected by the pH levels. They kept a water contact angle of ~160° with a contact angle hysteresis and rolling off-angle of <5°. However, this result does not indicate long-term stability of the surfaces against corrosive solutions.

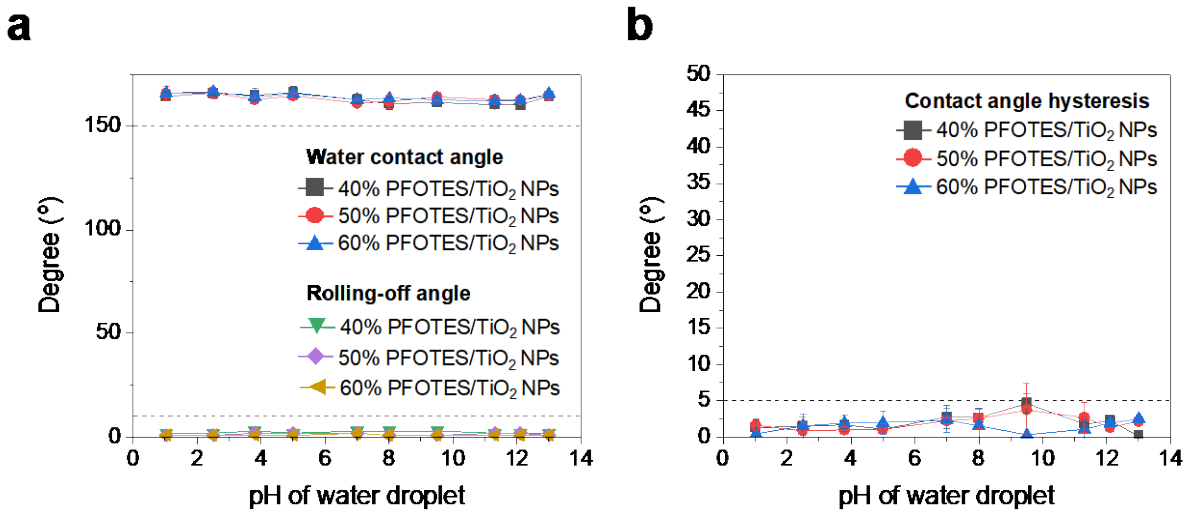

Fig. S15| pH stability of superhydrophobic surfaces containing 40, 50 and 60% PFOTES/TiO_2 NPs. a, Water contact and rolling off-angles. **b**, Contact angle hysteresis. The surface repellency to water droplets of pH 1–13 was investigated. Data presented as mean ± standard deviation.

Heat stability of superhydrophobic surface

Figure S16a-b represent the water contact angles, rolling off-angle, and contact angle hysteresis of superhydrophobic surfaces after heat exposure up to 180°C. The superhydrophobic surfaces were placed in a furnace and exposed to thermal energy ranging from 20 to 180°C. They were exposed to heat for 1 h at each condition. Despite heat exposure up to 180°C, they remained superhydrophobic, indicating that it is stable at 180°C. Figure S16c shows surface topographies before and after 1 h exposure to 180°C. Despite UHMWPE's melting point of 144–152°C, the microstructures on the composites remained after 1h exposure to 180°C, resulting in the

surfaces being superhydrophobic. This enhanced thermal stability may be due to the addition of the TiO_2 which has a transition temperature of over 1,000 ˚C. This enhanced thermal stability may be due to the addition of the TiO_2, which has a transition temperature of over 1,000 ˚C. Enhancing thermal stability by mixing materials with high thermal resistance has been well known. For example, Santos et al. (2011) reported that adding TiO_2 in a fluoride system improves the thermal parameters of the glass.[5] Stambouli et al. (2012) also demonstrated that the thermal stability of TeO_2-La_2O_3-TiO_2 glasses was enhanced with increasing TiO_2 compositio.[6] Laachachi et al. (2006) showed that the thermal stability of ammonium polyphosphate was particularly improved by the use of the oxide nanoparticles (Al_2O_3 and TiO_2).[7]

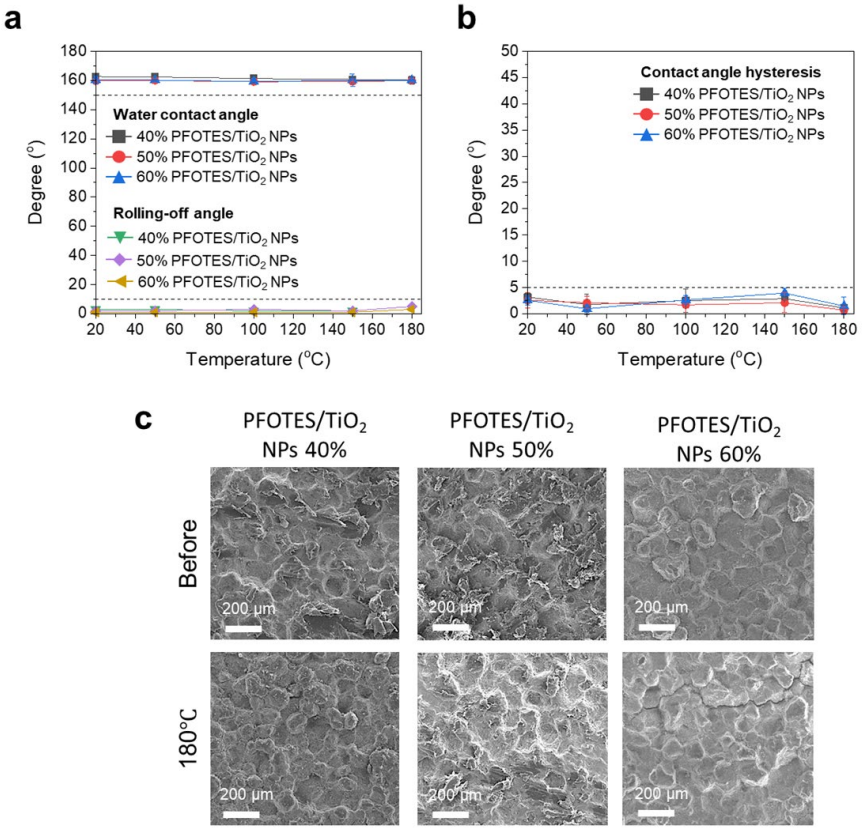

Fig. S16| Heat stability of superhydrophobic surfaces containing 40, 50 and 60% PFOTES/TiO_2 NPs. a, Water contact angle and rolling off-angle. **b**, Contact angle hysteresis. The samples were placed in a furnace and exposed to the thermal energy of 20–180ºC. At each condition, the samples were exposed to heat for 1 h. **c**, Surface topographies (SEM images) of composites containing 30, 40, 50, and 60% PFOTES/TiO2 NPs before and after the heat exposure at 180ºC. Data presented as mean ± standard deviation.

As shown in Figure S17, after exposure to extreme conditions, including surface burning, aqua regia, oil and paint, the nano/microstructures collapsed or coated. However, after the recovery process using sandpaper abrasion, the nano/microstructures were rebuilt.

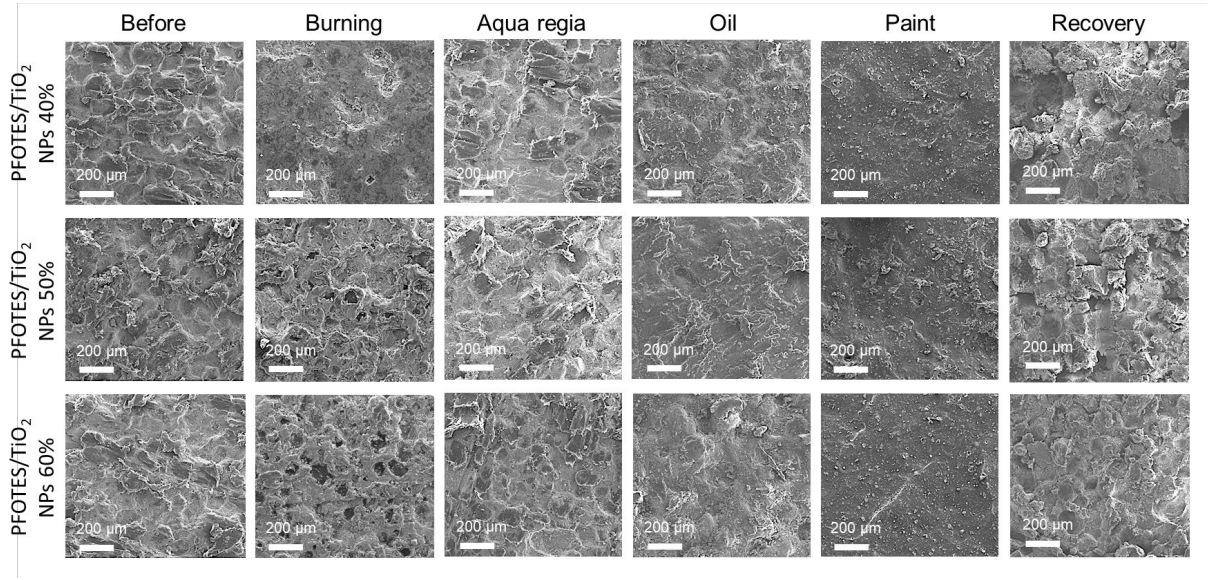

Fig. S17| Surface topographies (SEM images) of composites containing 3 40, 50 and 60% PFOTES/ TiO_2 NPs before and after exposure to the extreme conditions and the topographies after surface recovery using sandpaper.

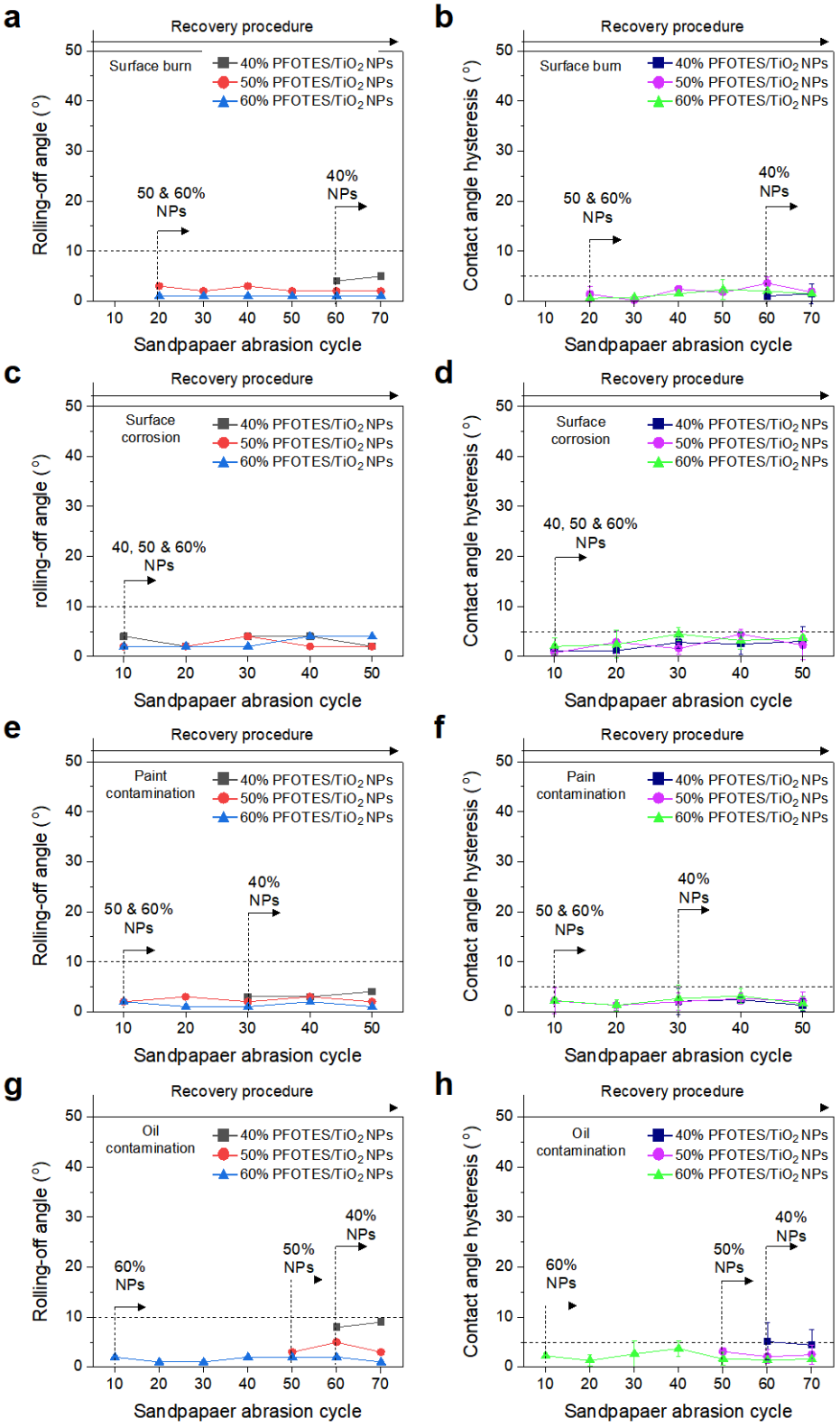

Fig. S18| Water rolling off-angle and contact angle hysteresis 40, 50, and 60% PFOTES/TiO_2 NPs after the recovery procedure. a-b, Surface burn by a flame at 2000°C. **c-d**, Surface corrosion by aqua regia. **e-h**, Paint and oil contaminations. Data presented as mean ± standard deviation.

Supplementary Note 5

A defibrinated horse blood, which is non-Newtonian fluid, was used in this study. The fluidic property of the blood is different from the Newtonian fluid, for example, water. Its viscosity changes by shear or tensile stresses. Previous showed that the superhydrophobic surface is susceptible to blood resulting in water repellency loss.[8, 9] As shown in Figure S19, it was also observed that the superhydrophobic surfaces were wet by the blood after dipping for 5 min. The water contact angle on the contaminated surface was between 76 and 85°, indicating the superhydrophobicity loss. However, all surfaces recovered superhydrophobicity with a water contact angle of ~160 ° and rolling off-angle and contact angle hysteresis of <5 ° after 10 cycles of the sandpaper abrasion. The sandpaper abrasion removed the bold contaminant and rebuilt the hydrophobic nano/microstructures on the surfaces.

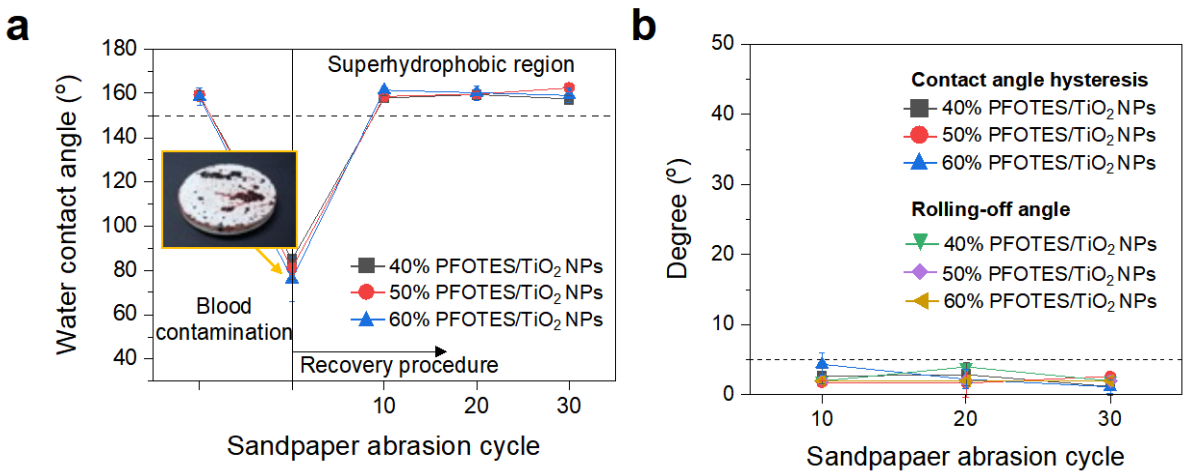

Fig. S19| Recovery of superhydrophobic surfaces containing 40, 50, and 60% PFOTES/TiO_2 after blood contamination. a, Water contact angle. **b**, Rolling off-angle and contact angle hysteresis. A defibrinated horse blood was used. Data presented as mean ± standard deviation.

Supplementary Note 6

Other types of superhydrophobic surfaces were tested under extreme conditions. NeverWet and Ultra-Ever Dry, which are commercial superhydrophobic surfaces, and superhydrophobic surfaces of Lu et *al*. (2015) and Chen et *al*. (2016), which have been known to be robust surfaces, were selected.[10,11] Superhydrophobic surfaces using NeverWet and Ultra Ever Dry sprays were produced in accordance with suppliers' guidance notes. A glass slide was coated with bottom spray and allowed to dry for 20 min, and then the slide was coated with top spray and dried for 30 min. To produce the surface of Lu et *al*. (2015), double-sided tape attached glass was dipped into superhydrophobic paint, collected, and allowed to dry for 4 h.[12] For the surface of Chen et al. (2016), a glass slide was coated with glue spray and then coated with a superhydrophobic solution containing calcium carbonate ($CaCO_3$), perfluorinated silane, and ethanol[11]. Figure S20a shows changes in the water contact angle of the tested surfaces under extreme conditions. Surface burning using a flame with a temperature of 2000 ^{o}C and silicone oil contamination significantly changes the water contact angle of all tested surfaces. The surface contact angles decreased to ~ 88^{o}. The sanding process was applied to the damaged or contaminated surfaces under a load pressure of 10−14 kPa to determine if the process recovers the hydrophobicity. When significant wear on the surface by the abrasion was observed, further recovery procedure was not conducted. As shown in Figure S20b−c, a significant increase in the water contact angle of all surfaces was not observed, indicating that recreating a superhydrophobic surface is required.

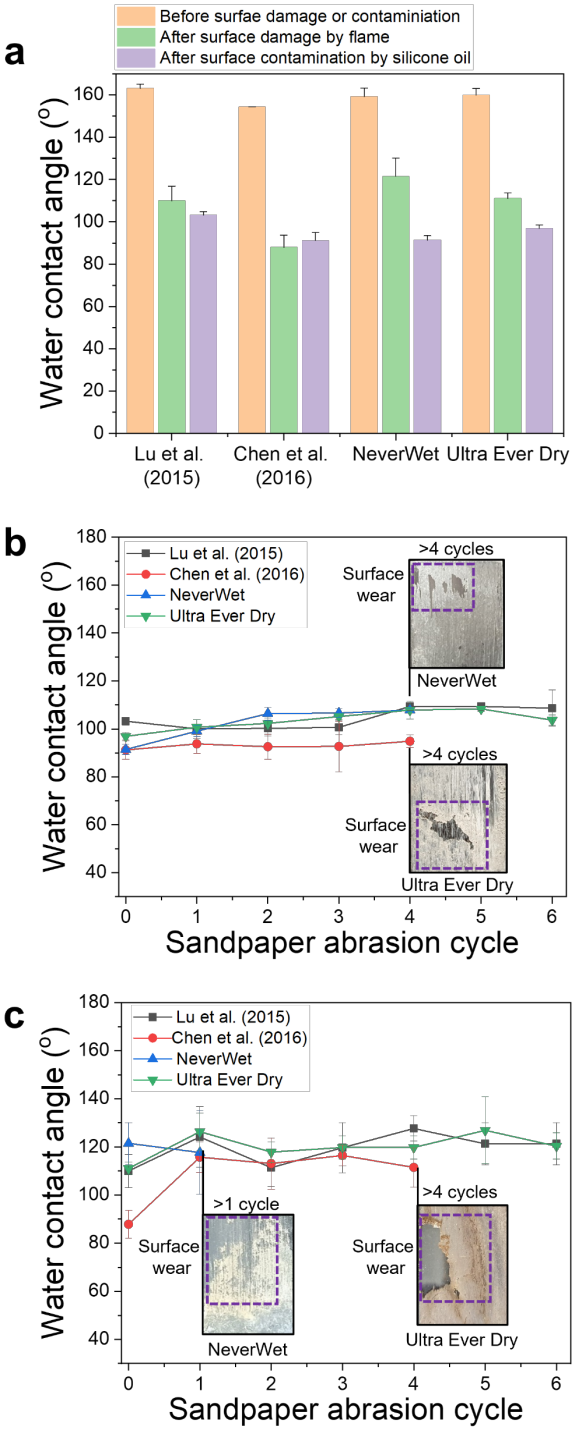

Fig. S20| Damage/contamination and recovery of tested surfaces. a, Change in water contact angle after surface burn by flame with a temperature of 2000°C and surface contamination by silicone oil coating. **b,** Recovery process after oil contamination**. c,** Recovery process after surface burn by flame with a temperature of 2000°C. Data presented as mean ± standard deviation.

Supplementary Note 7

To confirm the effect of the abrasive methods, superhydrophobic surfaces were fabricated by randomly directional abrasion with Grit No. 120 sandpaper. A randomised directional abrasion indicates that the abrasion direction is determined by randomly rotating the sample every 10 cycles, and 100 cycled abrasion was conducted to produce a superhydrophobic surface. Figure S20 shows the surface wettability depending on the different abrasion methods. Unidirectional refers to samples that were fabricated in our conventional way. The wettability measurement and SEM analysis showed that regardless of the abrasion direction, all samples have a water contact angle of >150^{o} with a rolling off angle of < 3^{o} and nan/microstructure was produced through the processes. In addition, another method using a sanding machine showed the surface became superhydrophobic after that treatment (Supplementary Video 8). This indicates that in our research, the abrasion direction is not an essential factor in producing superhydrophobicity.

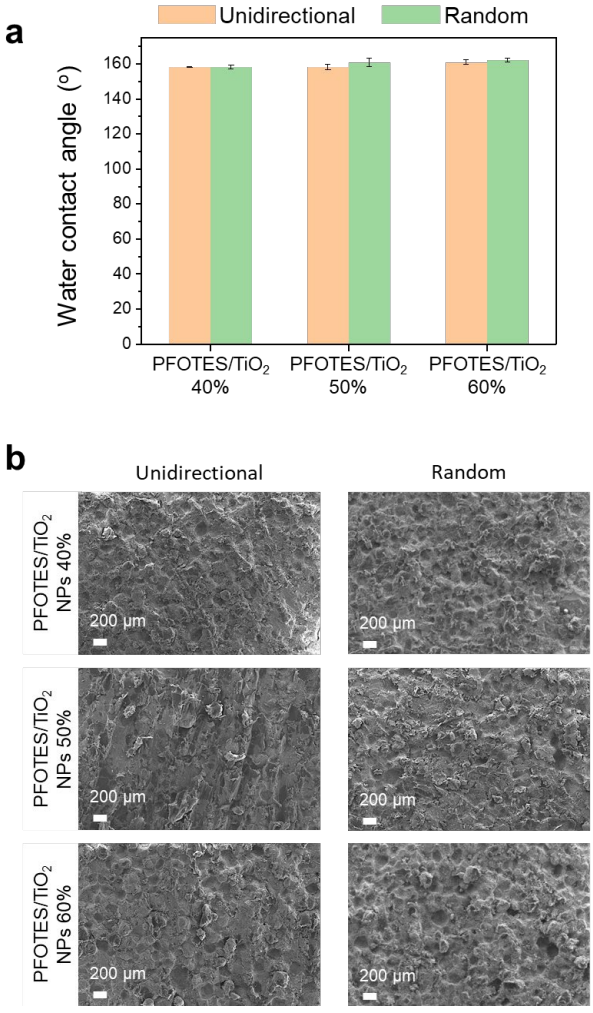

Fig. S21| Different abrasion method. a, Water contact angle depending on the abrasion method.

Rolling off-angle of all samples is less than 3°. **b,** Surface topographies (SEM images) of composites containing 30, 40, 50, and 60% PFOTES/TiO_2 NPs by different abrasive methods. Data presented as mean ± standard deviation.

References

1 R. Akid, M. May, H. M. J. Wang, *Eng. Appl. Sci.* 2015, **14**, 9-19.

2 B. E. Kanyanthare, , B. Asamoah, M. U. Ishaq, J. Amoani, J. Räty, K. E. Peiponen, *Chemosensors* 2020, **8**, 88.

3 I. A. Larmour, S. E. Bell, G. C. Saunders, *Angew. Chem.* 2007, **46**, 1710-1712.

4 G. B. Hwang, K. Page, A. Patir,, S. P. Nair,, E. Allan, I. P. Parkin, *ACS Nano* 2018, **12**, 6050-6058.

5 F. A. Santos, J. R. J. Delben, A. A. S. T. Delben, L. H. C. Andrade, S. M. Lima, *J. Non-Cryst. Solids* 2011, **357**, 2907-2910.

6 W. Stambouli, H. Elhouichet, M. Ferid, *J. Mol. Struct.* 2012, **1028**, 39-43.

7 A. Laachachi, E. Cochez, P. Leroy, M. Gaudon, J. M. Ferriol, L. Cuesta, *Polym. Adv. Technol.* 2006, **17**, 327-334.

8 T. S. Wong, S. H. Kang, S. K. Y. Tang, E. J. Smythe, B, D. Hatton, A. Grinthal, J. Aizenberg, *Nature* 2011, **477**, 443-447.

9 A. Patir, G. B. Hwang, C. Lourenco, S. P. Nair, C. J. Carmalt, I. P. Parkin, *ACS Appl. Mater. Interfaces.* 2021, **13**, 5478-5485.

10 Y. Lu, S. Sathasivam, J. Song, C. R. Crick, C. J. Carmalt, I. P. Parkin, *Science* 2015, **347**, 1132-1135.

11 B. Chen, J. Qiu, E. Sakai, N. Kanazawa, R. Liang, H. Feng, *ACS Appl. Mater. Interfaces* 2016, **8**, 17659-17667.

12 C. Zhiming, L. Shen, X. Wang, Q. Guo, *Compos. Sci. Technol.* 2018. **164**, 238-247.